

A Deep-Learning Enhanced Gappy Proper Orthogonal Decomposition Method for Conjugate Heat Transfer Problem

Arash Hajisharifi^{*†1}, Rahul Halder^{‡1}, Michele Girfoglio¹, Giovanni Stabile², and Gianluigi Rozza¹

¹Mathematics Area, mathLab, SISSA, via Bonomea 265, I-34136 Trieste, Italy

²Biorobotics Institute, Sant'Anna School of Advanced Studies, Piazza Martiri della Libertà, 33, 56127 Pisa, Italy

ABSTRACT

The current study aims to develop a non-intrusive Reduced Order Model (ROM) to reconstruct the full temperature field for a large-scale industrial application based on both numerical and experimental datasets. The proposed approach is validated against a domestic refrigerator. At the full order level, air circulation and heat transfer in fluid and between fluid and surrounding solids in the fridge were numerically studied using the Conjugated Heat Transfer (CHT) method to explore both the natural and forced convection-based fridge model followed by a parametric study-based on the ambient temperature, fridge fan velocity, and evaporator temperature. The main novelty of the current work is the introduction of a stable Artificial Neural Network (ANN) enhanced Gappy Proper Orthogonal Decomposition (GPOD) method which shows better performance than the conventional GPOD approach in such large-scale industrial applications. The full-order model is validated with the experimental results and the prediction accuracy of the surrogate model associated with different reduced-order approaches is compared with the benchmark numerical results or high-fidelity results. In our current work, we show that a prediction error of 1 ($^{\circ}\text{C}$) and computational speed-up of $5e3$ is achieved even at a very sparse training dataset using the proposed deep-learning enhanced GPOD approach.

Keywords: Conjugate Heat Transfer (CHT), Proper Orthogonal Decomposition (POD), Gappy POD, Artificial Neural Network (ANN)

1 Introduction

Significant research has been carried out on ROM in the last few decades. Its application ranges in several industrial practices such as aerospace [43, 47], pharmaceuticals [26, 25], marine engineering [15, 16] and even home appliances industries [12, 6, 55].

Domestic refrigerator system is one key application of conjugate heat transfer problems driven by forced and natural convection. Maintaining the prescribed limit of the temperature fields inside different compartments is one of the key criteria of the domestic refrigerator design to ensure energy efficiency and freshness of food.

Several research works on heat transfer in an enclosed chamber such as work by Markatos et al.[34] provide the necessary numerical tools required for the development of the full computational fluid dynamics-based domestic fridge model governed by natural convection. A full-scale domestic fridge with natural convection was modeled by Laguerre and Flick [31]. Numerical simulation considering the radiation effect was carried out in their later work [30]. Söylemez et al. [51] considered forced convection arising due to the fan velocity inside a domestic refrigerator. However, in their numerical model, only the fluid volume was considered neglecting the heat transfer in the solid region of the refrigerator. Zhang and Lian [58] considered the conjugate heat transfer

^{*}These author(s) contributed equally to this work.

[†]Emails: ahajisha@sissa.it, rhalder@sissa.it, mgirfogl@sissa.it, giovanni.stabile@santannapisa.it, grozza@sissa.it

[‡]These author(s) contributed equally to this work.

(CHT) algorithm to account for heat transfer in both the fluid and solid regions of the domestic refrigerator model. However, there are several research works carried out to numerically model a domestic refrigerator, there is limited work considering all the relevant physics associated with the system such as conjugate heat transfer, natural and forced convection, radiation heat transfer and turbulence.

The full-order numerical model associated with the domestic refrigerator is numerically expensive especially when there are repetitive tasks involved such as in the design step, process optimization, and development of control algorithm. The reduced order model approach facilitates the exploration of parametric space while carrying out those repetitive tasks in industrial practice. In general, the reduced order model consists of two steps - one is the offline phase where the high-fidelity simulation is carried out using high-performance computing in clusters at several parametric points to develop the solution manifolds. The second stage is online usually performed on a less powerful machine such as personal laptops. At this online phase when the parametric space and transient dynamics are learnt using surrogate models such as a data-driven approach, the class of those reduced order approaches is usually termed as a non-intrusive reduced order model. A variety of data-driven ROM techniques have been proposed in recent years, including interpolation-based and machine-learning-based approaches [24, 23, 25]. In heat-transfer applications, non-intrusive ROMs have also been coupled with Bayesian inversion and data assimilation to infer unmeasured boundary fluxes and temperature in real time [2].

Gappy data reconstruction implies the completion of the full field variables with partial experimental data at the sensors' location. Several interpolations and least-square estimations have been instrumental in the literature for the approximation of the missing data. Optimal interpolation approach has been used by Reynolds et al. [42], Smith et al. [50], Kaplan et al.[28]. The kriging approach [39] is used for the evaluation of the missing points using local weighted averaging. Everson and Sirovich [17] proposed an approach combining the Proper Orthogonal Decomposition (POD) with the least-square estimation for the reconstruction of "gappy" or missing data. The gappy POD approach has been used for several applications for the reconstruction of the full flowfield using experimental and numerical data at the sensor points such as in the case of the aerospace application by Bui-Thanh et al. and Wilcox [9, 54], cavity flow [37], boundary layers [22], biomedical application [56]. An algorithm based on frequency-domain, or spectral proper orthogonal decomposition (SPOD), for gappy data reconstruction, was proposed by Nekkanti et al. [38]. Recently, several deep-learning-based approaches have been considered for the reconstruction of the flow field using nonlinear methods like convolution neural networks (CNN) [48] and generative adversarial networks [57]. However, there are limited works on the employment of such a deep-learning approach for the use of both high-fidelity numerical data and experimental data (at the sensor locations).

In this study, we introduce a novel non-intrusive reduced-order modeling (ROM) approach that integrates data-driven techniques like POD-ANN (Proper Orthogonal Decomposition combined with Artificial Neural Networks) with the traditional Gappy POD method. This approach is termed as ANNGPOD. This hybrid framework reconstructs the full-field variable using numerical simulations at multiple parametric points alongside sparse sensor data. The proposed method exhibits strong robustness and delivers accurate predictions of the temperature field, irrespective of the number or placement of the sensor points. Furthermore, Proper Orthogonal Decomposition coupled with Radial Basis Function (POD-RBF) based ROM approach is also applied to the refrigerator CFD model to explore the parametric space and compared with the proposed ANNGPOD method. Here, only the high-fidelity numerical data set is considered.

We organise the current work in the following way: Section 2 describes the full-order CFD model associated with the domestic fridge model. The reduced order model based on the POD-RBF approach, conventional GPOD method and our proposed deep learning enhanced GPOD method termed ANNGPOD are described in Section 3. Finally, the numerical results associated with the full-order model and reduced order model are discussed in Sections 4 and 5. At the end of Section 5 we have introduced the computational speed-up due to different ROM approaches.

2 The full order model

A conjugate heat transfer (CHT) algorithm is used to carry out the steady-state Reynolds-Averaged Navier-Stokes (RANS) simulations. This method is based on solving the conservation of mass, momentum and energy in fluid and the conservation of energy in solid, simultaneously [58, 29,

33, 21, 32]. To ensure the continuity of temperature, the fluid and solid region are coupled by exchanging the information at the fluid-solid, solid-solid interfaces. The governing equations in the fluid region are described in Sec. 2.1, while the governing equation in the solid region is presented in Sec. 2.2.

2.1 Governing equations for fluid

The steady-state motion of compressible fluid in a spatial domain of interest Ω_f is described by Navier-Stokes equations:

$$\frac{\partial \rho u_j}{\partial x_j} = 0 \quad \text{in } \Omega_f, \quad (1)$$

$$\frac{\partial}{\partial x_j} (\rho u_i u_j) = -\frac{\partial p'}{\partial x_i} + \frac{\partial}{\partial x_j} (\mu \frac{\partial u_i}{\partial x_j}) + \frac{\partial}{\partial x_j} (-\rho u'_i u'_j) \quad \text{in } \Omega_f, \quad (2)$$

where ρ is density, u represent the mean velocity and u' represent the fluctuating velocity. μ is the dynamic viscosity and p' is the modified pressure, defined as:

$$p' = p + \frac{2}{3}\rho k + \frac{2}{3}(\mu + \mu_t) \frac{\partial u_k}{\partial x_k}, \quad (3)$$

where p is the pressure, μ_t is the eddy viscosity and k turbulent kinetic energy. The subscript i , j and k denote the velocity component in the x_i , x_j and x_k directions, respectively. The last term in 2, represents Reynolds stress tensor, τ_{ij} , which is defined as follows:

$$\tau_{ij} = \rho u'_i u'_j = -2\mu_t \left(S_{ij} - \frac{1}{3} \frac{\partial u_k}{\partial x_k} \delta_{ij} \right) + \frac{2}{3} \rho k \delta_{ij}, \quad (4)$$

where

$$S_{ij} = \frac{1}{2} \left(\frac{\partial u_i}{\partial x_j} + \frac{\partial u_j}{\partial x_i} \right) \quad (5)$$

In this study, we employed a two-equation eddy-viscosity turbulence model where μ_t is determined using $k - \omega$ SST model. In this model, the following two transport equations are solved for the dissipation rate, denoted as ω , and turbulent kinetic energy, k , [36, 46, 53, 1]:

$$\frac{\partial(\rho u_j k)}{\partial x_j} = \mathcal{P} - \beta^* \rho \omega k + \frac{\partial}{\partial x_j} \left[(\mu + \sigma_k \mu_t) \frac{\partial k}{\partial x_j} \right], \quad (6)$$

$$\frac{\partial(\rho u_j \omega)}{\partial x_j} = \frac{\gamma \rho}{\mu_t} \mathcal{P} - \beta \rho \omega^2 + \frac{\partial}{\partial x_j} \left[(\mu + \sigma_\omega \mu_t) \frac{\partial \omega}{\partial x_j} \right], \quad (7)$$

where the constants are $\beta^* = 0.09$, $\sigma_k = 0.5$, $\gamma = 5/9$, $\beta = 3/40$ and $\sigma_\omega = 0.5$. The production term \mathcal{P} is given by :

$$\mathcal{P} = -\tau_{ij} \frac{\partial u_i}{\partial x_j} \quad (8)$$

Given the significant temperature difference between the upper and lower parts of the computational domain considered in this study, we adopted a compressible ideal gas model. The energy equation for fluid region reads as:

$$\frac{\partial}{\partial x_i} (u_i (\rho \mathbf{E} + p)) = \frac{\partial}{\partial x_j} \left(\alpha_f \frac{\partial T_f}{\partial x_j} + u_i \frac{\partial}{\partial x_j} \left(\mu \frac{\partial u_i}{\partial x_j} - \rho u'_i u'_j \right) \right) + Q_r \quad \text{in } \Omega, \quad (9)$$

where \mathbf{E} is the total energy, α_f the fluid thermal diffusivity, T_f temperature in the fluid region and Q_r the heat source or sink due to the presence of radiation. Radiation, which has been demonstrated to play an important role in CHT simulations [58, 4, 30, 6], was modeled in our analysis by using Surface-to-Surface (S2S) model [19, 7]. This model approximates the expensive computation of radiation between surfaces to cheaper calculations. S2S model partitions the participating surfaces into discrete sections known as *view factors*. It computes the radiative heat flux by considering the temperature and emissivity of the surfaces, as well as their geometrical relationship. In this model, each surface is treated as both a source and sink of radiation, with its

emissivity and absorptivity assumed to be equal and constant [19]. The net energy leaving surface A due to radiation can be defined as the sum of radiative heat flux of each discrete surface, A_k , as follows:

$$Q_r = \sum_k \int_{A_k} q_k dA, \quad (10)$$

where A_k is the area of surface k . The radiative heat flux leaving surface k , denoted as q_k , is computed as follows [27, 35, 10] :

$$q_k = \epsilon_k \sigma T_{s,k}^4 + \mathcal{R}_k \sum_{j=1}^N F_{k,j} q_j, \quad (11)$$

where q_j represents the radiative heat flux from the surroundings surface, $\sigma = 5.67 \times 10^{-8} w/(m^2 K^4)$ is the Stefan-Boltzmann constant, $T_{s,k}$ is the temperature of surface k , ϵ_k and \mathcal{R}_k represent the surface emissivity and reflectivity, respectively. The view factor $F_{k,j}$ indicates the fraction of radiation that leaves surface k and hits surface j . This factor is a function of the geometric configuration and orientation of the surfaces [11, 7].

2.2 Governing equations for solid

The governing equation for conductive heat transfer in the solid region in a domain of interest Ω reads as:

$$\frac{\partial}{\partial x_j} \left(\alpha_s \frac{\partial T_s}{\partial x_j} \right) = 0 \quad \text{in } \Omega, \quad (12)$$

where T_s is the temperature in solid region and $\alpha_s = \lambda / (\rho C_p)$ is the thermal diffusion coefficient. λ , ρ_s and C_p are thermal conductivity, density, and specific heat of solid, respectively.

We used the second-order accurate finite volume method (FVM), implemented in the open-source C++ library OpenFOAM®[52], to discretize the partial differential equations. The Semi-Implicit Method for Pressure Linked Equations (SIMPLE) algorithm was used to couple pressure and velocity [40]. In this algorithm, a prediction step followed by a correction step is used to couple pressure and velocity fields.

3 Reduced order model

In this section, we introduce a novel non-intrusive parametric reduced-order model that reconstructs the temperature fields at regions of interest in a domestic refrigerator, leveraging high-fidelity numerical data at known parameter values together with sparse experimental measurements from sensors at an unknown parameter value. A suitable training dataset is the first requirement for developing the reduced-order model. Section 3.1 introduces Proper Orthogonal Decomposition with Radial Basis Function interpolation (POD-RBF), and Section 3.2 presents its extension with Artificial Neural Networks (POD-ANN). The conventional Gappy Proper Orthogonal Decomposition (GPOD) is then introduced in Section 3.3. Next, we introduce ANNGPOD, a stable ANN-augmented GPOD method that extends POD-ANN by enriching its loss function with an additional term derived from the GPOD formulation, as described in Section 3.4.

3.1 POD with Radial Basis Function

We assume that any physical variable, such as temperature in the present case, can be approximated as a linear combination of basis functions ϕ (depending only on the spatial variable \mathbf{x}), weighted by scalar coefficients $\boldsymbol{\alpha}$ that depend on parameters (physical or geometrical) and/or time. Accordingly, the temperature field (T) and its reduced approximation (T_r) can be expressed as:

$$T \approx T_r = \sum_{i=1}^{N_T^r} \boldsymbol{\alpha}_i(t, \boldsymbol{\mu}) \phi_i(\mathbf{x}), \quad (13)$$

where N_T^r denotes the cardinality of the reduced basis of the temperature field, while t and $\boldsymbol{\mu}$ represent time and the parameter vector, respectively. In this work, we focus exclusively on parametric variations, where the parameter vector consists of the evaporator temperature T_{ev} , ambient temperature T_{amb} , and fan velocity percentage v_f . Now, to construct the reduced-order model, we employ Proper Orthogonal Decomposition (POD) combined with Radial Basis Function interpolation, known as the POD-RBF approach. The method involves two stages: offline and online. In the offline stage, a linear subspace is obtained via POD along with the corresponding reduced coefficients. Interpolation methods such as those in [13, 14, 5, 20, 26] are then used to learn the dependence of the reduced coefficients on the parameters, enabling efficient exploration of the parametric space during the online stage. Complementary to GPOD, Ensemble Kalman-type data assimilation can jointly estimate states and parameters from sparse sensors in fluid systems, improving near-wall or boundary reconstructions [3].

The algorithm begins with a collection of temperature field vectors, referred to as the snapshot matrix \mathbf{T} , associated with parameter values $\boldsymbol{\mu}_i$ (see Eqn. 14). Here, N_{dof} denotes the number of degrees of freedom of the full-order model, and M is the total number of parameter values considered:

$$\mathbf{T} = \begin{bmatrix} T_1(\mathbf{x}) & T_2(\mathbf{x}) & \dots & T_M(\mathbf{x}) \end{bmatrix} \in \mathbb{R}^{N_{dof} \times M}, \quad T_i(\mathbf{x}) = T(\mathbf{x}, \boldsymbol{\mu}_i), \quad i = 1, \dots, M. \quad (14)$$

where $\boldsymbol{\mu} \in \Omega_\mu \subset \mathbb{R}^M$ is the vector containing the associated parameter values $\boldsymbol{\mu}_i$. Applying Singular Value Decomposition (SVD) to the matrix \mathbf{T} yields:

$$\mathbf{T} = \mathbf{U} \boldsymbol{\Sigma} \mathbf{V}^T. \quad (15)$$

where, $\mathbf{U} \in \mathbb{R}^{N_{dof} \times N_{dof}}$, and $\mathbf{V} \in \mathbb{R}^{M \times M}$ are the matrices comprising of the left and right singular value vectors respectively. $\boldsymbol{\Sigma} \in \mathbb{R}^{N_{dof} \times M}$ is a matrix containing the singular values σ_i . $\mathbf{U}_{N_T^r}$ is the matrix \mathbf{U} truncated to the first N_T^r columns representing our POD space. The POD basis $\mathbf{U}_{N_T^r}$ minimizes $\|\mathbf{T} - \mathbf{U}_{N_T^r} \mathbf{U}_{N_T^r}^T \mathbf{T}\|_F$ where $\|\cdot\|_F$ is the Frobenius norm. Typically, the value of N_T^r is commonly chosen to meet a user-provided threshold δ for the cumulative energy of the singular values defined as:

$$\frac{\sum_{i=1}^{N_T^r} \sigma_i^2}{\sum_{i=1}^{N_s} \sigma_i^2} \geq \delta. \quad (16)$$

After constructing the POD space, we can approximate the input snapshots by using Eqn. 13.

$$T_r(\boldsymbol{\mu}_j) \approx \sum_{L=1}^{N_T^r} \mathbb{A}_L(\boldsymbol{\mu}_j) \phi_L, \quad \text{with} \quad j = 1, \dots, M, \quad (17)$$

where the modal coefficients, $\mathbb{A}_L(\boldsymbol{\mu}_j)$ are the elements of the matrix $\mathbf{C} = \mathbf{U}_{N_T^r}^T \mathbf{T} \in \mathbb{R}^{N_T^r \times N_{dof}}$. Then the ROM is built using as input-output data the pairs $\{(\boldsymbol{\mu}_j), \mathbb{A}_L(\boldsymbol{\mu}_j)\}$ associated to the L^{th} POD mode ϕ_L with $L = 1, \dots, N_T^r$.

where,

$$\mathbb{A}_L(\boldsymbol{\mu}_j) = \sum_{n=1}^M w_{L,n} \zeta_{L,n} (\|(\boldsymbol{\mu}_j) - (\boldsymbol{\mu}_n)\|), \quad (18)$$

Here, $\zeta_{L,n}$ are the Radial Basis Functions [8], which we chose as Gaussian functions centred in $(\boldsymbol{\mu}_n)$ and $w_{L,n} \in \mathbb{R}^M$ are unknown weights. Eqn. (18) can be reformulated in terms of a linear system :

$$\mathbf{Z}_L \mathbf{w}_L = \mathbb{A}_L, \quad (19)$$

to be solved to obtain the weights \mathbf{w}_L for every value of $L = 1, \dots, N_T^r$ once at all in the offline phase. Matrix, \mathbf{Z}_L consists of the radial basis functions values.

Then, in the online phase, for any new parameter, $(\boldsymbol{\mu}_*)$, the approximated modal coefficients, $\mathbb{A}_L(\boldsymbol{\mu}^*)$, are calculated from Eqn. 18 and the ROM solution is computed as:

$$T_r(\boldsymbol{\mu}_*) = \sum_{L=1}^{N_T^r} \mathbb{A}_L(\boldsymbol{\mu}_*) \phi_L. \quad (20)$$

3.2 Artificial Neural Network

An ANN is a deep learning model consisting of neurons and a set of directed weighted synaptic connections among the neurons. ANN is an oriented graph, with the neurons as nodes and the synapses as oriented edges. The weights associated with the ANN are adjusted by employing a training process to configure the network for a specific application. Let us consider the neuron j . Three functions characterize completely the neuron j :

- the propagation function u_j is used to transport values through the neurons of the ANN. m is the total number of sending neurons linked with the neuron j . The weighted sum approach is used where b_j is the bias, y_{sk} is the input related to the sending neuron k , and w_{sk} are the weights.

$$u_j = \sum_{k=1}^m w_{sk,j} y_{sk} + b_j. \quad (21)$$

- the activation function f_{act} which operates on u_j during the training process:

$$a_j = f_{\text{act}, j} \left(\sum_{k=1}^m w_{sk,j} y_{sk} + b_j \right). \quad (22)$$

Commonly the activation functions are non-linear. Possible choices are sigmoid function, hyperbolic tangent, RELU, SoftMax. More details can be found in [49].

- the output function y_j . It is related to the activation function a_j . Often it is the identity function, so that a_j and y_j coincide:

$$y_j = f_{\text{out}}(a_j) = a_j. \quad (23)$$

In this work, we will use a specific type of ANN, the feedforward neural network [18] with multiple layers. In a feedforward neural network, each node in one layer is connected to all nodes in subsequent layers. We highlight that the input layer of our network consists of the set of time/parameter instances $\{(\boldsymbol{\mu}_1), \dots, (\boldsymbol{\mu}_M)\}$ whilst the output one is given by the corresponding modal coefficients $\mathbb{A}_L(\boldsymbol{\mu}_1), \dots, \mathbb{A}_L(\boldsymbol{\mu}_M)$, with $L = 1, \dots, N_T^r$. During the training procedure, the weights of the connections in the network are repeatedly changed to minimize the difference between the output vector of the net $\tilde{\mathbb{A}}_L$ and the required output vector \mathbb{A}_L using backpropagation algorithm [44, 45]. The key to backpropagation is a method for computing the gradient of the error concerning the weights for a given input by propagating the error backwards through the network. A loss function is introduced to optimize the parameter values in a neural network model. The loss function $\mathcal{L} = \mathcal{L}(\tilde{\mathbb{A}}_L, \mathbb{A}_L)$ used in this work is the mean squared error (MSE), which is the most common choice for regression problems:

$$\mathcal{L}_{\text{ANN}} = \frac{1}{M} \sum_{i=1}^M \mathcal{L}_i = \frac{1}{M} \sum_{i=1}^M \frac{1}{L} \sum_{j=1}^L \left(\mathbb{A}_{i,j} - \tilde{\mathbb{A}}_{i,j} \right)^2 \quad (24)$$

3.3 Gappy POD

The conventional Gappy POD approach computes the temperature field based on temperature sensor data available at a few sensor locations, termed as missing or "gappy" data. A brief description of the Gappy POD approach is described in the current subsection. First, a mask matrix is developed to locate the rows where the data is available. For the temperature field prediction, the corresponding mask vector l^k is as follows:

$$\begin{aligned} l^k &= 0 \text{ if } T^i(\boldsymbol{\mu}_k) \text{ is missing,} \\ l^k &= 1 \text{ if } T^i(\boldsymbol{\mu}_k) \text{ is known,} \end{aligned} \quad (25)$$

where, $T^i(\boldsymbol{\mu}_k)$ denotes the i^{th} element of the vector $T(\boldsymbol{\mu}_k)$, pointwise multiplication is defined as $(l^k, T(\boldsymbol{\mu}_k))^i = l^{i,k} T^i(\boldsymbol{\mu}_k)$. The inner product and induced norm can be expressed respectively as shown in Eqn. 26:

$$(z, v)_l = ((l, z), (l, v)), \quad (\|v\|)^2 = (v, v)_l \quad (26)$$

As discussed in the previous section, the standard POD basis vector is defined as ϕ_L for the known snapshots set $T(\mathbf{x}, \boldsymbol{\mu}_k)$ where $k = 1$ to M and $L = 1$ to N_T^r .

Now assume, at an unknown parameter, $\boldsymbol{\mu}^*$, partial data is available

$$\hat{T}_{\boldsymbol{\mu}^*} = [\hat{T}(\hat{\mathbf{x}}, \boldsymbol{\mu}^*)] = (l, [T(\mathbf{x}, \boldsymbol{\mu}^*)]) \in \mathbb{R}^{N_{\text{dof,partial}}}, \quad (27)$$

where \hat{T} is the partial temperature data available at locations $\hat{\mathbf{x}}$ and parameter $\boldsymbol{\mu}^*$. $N_{\text{dof,partial}}$ is the dimension of the sparse dataset available. In the next step, we need to obtain the reduced truncated basis Φ_R to solve a set of linear equations to minimise the following \mathcal{L}_{GPOD} shown in Eqn. 28.

$$\mathcal{L}_{GPOD} = \hat{T}_{\boldsymbol{\mu}^*} - \sum_{L=1}^{N_T^r} \mathbb{A}_L(\boldsymbol{\mu}^*) \phi_{R,L}(\hat{\mathbf{x}}) \quad (28)$$

where, $\Phi_R = [\phi_{R1}, \phi_{R2}, \dots, \phi_{RL}]$, $\phi_{Ri} = (l, \phi_i)$. Φ_R is not orthonormal anymore after the selected rows are omitted. If the number of points where data is available and the number of modes are not the same, in that case, the matrix Φ_R is rectangular. Therefore, Eqn. 28 is solved by computing the pseudo-inverse of the matrix Φ_R as shown in Eqn. 29.

$$\mathbb{A}(\boldsymbol{\mu}^*) = [\Phi_R]^\dagger \hat{T}_{\boldsymbol{\mu}^*}, \dagger \text{ is the pseudo-inverse of a rectangular matrix} \quad (29)$$

3.4 Deep Learning enhanced Gappy POD

We propose a deep learning enhanced Gappy POD approach introducing additional loss terms arising from Gappy POD i.e., Eqn. 28 in the loss term associated with the POD-ANN approach, Eqn 24. Now we will describe the inputs and outputs of our proposed method ANNGPOD. The Input layer of ANNGPOD consists of the set of parameter values $\{(\boldsymbol{\mu}_1), \dots, (\boldsymbol{\mu}_M)\}$. The objective is to reconstruct the temperature field at $\boldsymbol{\mu}^*$ where sparse measurements of temperature \hat{T}_* are available which acts as additional input to the ANNGPOD network. The output is given by the corresponding modal coefficients $\mathbb{A}_L(\boldsymbol{\mu}_1), \dots, \mathbb{A}_L(\boldsymbol{\mu}_M)$, with $L = 1, \dots, N_T^r$. Following are the steps of the ANNGPOD.

- At every epoch iteration, the prediction of the POD-ANN network at $\boldsymbol{\mu}^*$ is $\tilde{\mathbb{A}}_{i,j=^*}$ with $i = 1, \dots, N_T^r$
- The temperature field can be computed from the $\tilde{\mathbb{A}}_{i,j=^*}$ as follows:

$$\tilde{T}_r(\boldsymbol{\mu}^*) = \sum_{i=1}^{N_T^r} \tilde{\mathbb{A}}_i(\boldsymbol{\mu}^*) \phi_i \quad (30)$$

- Additional loss term arising from sparse measurement data at location $(\hat{\mathbf{x}}_i)$ can be computed as:

$$L_{GPOD} = \frac{1}{N_{\hat{\mathbf{x}}}} \sum_{i=1}^{N_{\hat{\mathbf{x}}}} (\hat{T}_{\boldsymbol{\mu}^*}(\hat{\mathbf{x}}_i) - \tilde{T}_r(\boldsymbol{\mu}^*, \hat{\mathbf{x}}_i))^2 \quad (31)$$

where, $N_{\hat{\mathbf{x}}}$ is the total number of sensors where measurement data is available.

- The total loss term associated with the ANNGPOD network which goes into the backpropagation algorithm to update the weight matrix and bias vectors in the next epoch iteration is as follows:

$$L_{ANNGPOD} = \lambda_1 \frac{1}{M} \sum_{i=1}^M \frac{1}{L} \sum_{j=1}^L \left(\mathbb{A}_{i,j} - \tilde{\mathbb{A}}_{i,j} \right)^2 + \lambda_2 \frac{1}{N_{\hat{x}}} \sum_{i=1}^{N_{\hat{x}}} (\hat{T}_{\mu_*}(\hat{x}_i) - \tilde{T}_r(\mu_*, \hat{x}_i))^2 \quad (32)$$

The constants, λ_1 and λ_2 are associated with the loss term arising from the POD-ANN and GPOD method, respectively.

We explain the steps of the ANNGPOD method in the following pseudo-code. Furthermore, We like to mention that POD-RBF approach mentioned in Section 3.1 can be coupled with the Gappy POD to improve the performance of the conventional Gappy POD method, however, in ANN or any deep learning framework, loss terms can be easily modified and such flexibility in the implementation step has motivated the choice of the current regression method, POD-ANN to demonstrate the proposed approach for a practical industrial applications.

Algorithm 1: pseudo-code for ANNGPOD Algorithm

```

Data:  $\mathbf{u} = \{(\mu_1), \dots, (\mu_M)\}, \mathbb{A}_L(\mu_1), \dots, \mathbb{A}_L(\mu_M)$ , with  $L = 1, \dots, N_T^r$ ,  $\tilde{T}_{\mu_*}$ 
1  $[W, b] \leftarrow \text{INIT}([W, b])$ ; /* Initialize Weight and bias */
2 while epoch  $\leq$  Total Epoch No. do
3    $\tilde{\mathbb{A}}_{i,j}, i = 1, L, j = 1, M \leftarrow \text{NN}(W, b, f_{\text{act}}, \mathbf{u})$ ; /* prediction from chosen network
   NN */
4    $L_{\text{POD-ANN}} \leftarrow \frac{1}{M} \sum_{i=1}^M \frac{1}{L} \sum_{j=1}^L \left( \mathbb{A}_{i,j} - \tilde{\mathbb{A}}_{i,j} \right)^2$ ; /* compute POD-ANN based loss
   term */
5    $\tilde{\mathbb{A}}_{i,j=\ast} \leftarrow \text{NN}(W, b, f_{\text{act}}, \mu_*)$ ; /* prediction from the net at parameter  $\mu_*$  */
6    $\tilde{T}_r(\mu_*) \leftarrow \sum_{L=1}^{N_T^r} \tilde{\mathbb{A}}_L(\mu_*) \phi_L$ ; /* Reconstruct the temperature field at  $\mu_*$  */
7    $L_{\text{GPOD}} \leftarrow \frac{1}{N_{\hat{x}}} \sum_{i=1}^{N_{\hat{x}}} (\hat{T}_{\mu_*}(\hat{x}_i) - \tilde{T}_r(\mu_*, \hat{x}_i))^2$ ; /* Compute the loss term based on
   GPOD */
8    $L \leftarrow (L_{\text{POD-ANN}} + L_{\text{GPOD}})$ ; /* compute total loss term for backpropagation
   */
9    $\Delta W \leftarrow -\alpha \text{GADAM}(\nabla_W L), \Delta b \leftarrow -\alpha \text{GADAM}(\nabla_b L)$ ;
   ; /* compute weight matrices and bias vector update */
10   $W \leftarrow W + \Delta W, b \leftarrow b + \Delta b$ ;

```



Figure 1: Sketch of the computational domain: the left and right panels illustrate the side and front views of the geometry. The sub-panel highlights the fan region and its configuration.

4 Numerical results

In this work, we studied a household fridge with dimensions $1205 \times 510 \times 485$ mm. Fig. 1 illustrates the side and front views of the fridge under investigation on the right and left panels, respectively. The fridge includes the following components essential for its functionality: door bins which are located on the fridge door, a crisper and a drawer positioned at the bottom of the fridge to store food items with humidity controls for preservation. Moreover, there are liners and gaskets designed to contribute to the insulation by creating an airtight closure. The foam insulation surrounds the inner cavity to minimize the heat transfer to and from the environment. Furthermore, there are 4 shelves to separate the inner cavity space and a fan located at the top of the fridge. The fan is covered by a frame as highlighted in the sub-panel of Fig. 1. The thermal behavior of the fridge is monitored by 26 temperature sensors located in various locations of the fridge. The sensors are modeled as solid cylinders with a height of 12 mm and a radius of 5 mm.

The entire domain is divided into fluid and solid regions to form the computational domain for CHT simulation. The fluid region represents the air inside the fridge compartment, whereas the solid regions represent the various components of the fridge such as the door bins, crisper, drawer, sensors and others. Different material properties like density, specific heat, and thermal conductivity are defined for each region to accurately model the thermal behavior of each region. Solid-fluid or solid-solid regions interact thermally with each other by exchanging information through interfaces.

The convective heat transfer boundary condition was applied to the external surfaces of the fridge to model the heat transfer between the outer solid and the environment fluid, using a fixed heat transfer coefficient, $h = 4 \text{ W}/(\text{m}^2\text{K})$. The temperature coupling boundary condition was applied to both fluid-solid and solid-solid interfaces. This boundary condition links the temperature of adjacent domains at their interfaces to accurately model the heat transfer in CHT simulations. The no-slip boundary condition was imposed on all the interfaces between air and solid components. Furthermore, we set the fixed temperature boundary condition for the fridge evaporator. This component acts as the cooling source to lower the temperature of its adjacent solid, which is the inner liner of the fridge. Consequently, the inner liner, that surrounds the air, cools down the air. An accurate CHT simulation requires a conformal multi-region mesh. The multi-region mesh, where separate meshes are generated for each region, is necessary for CHT simulations as

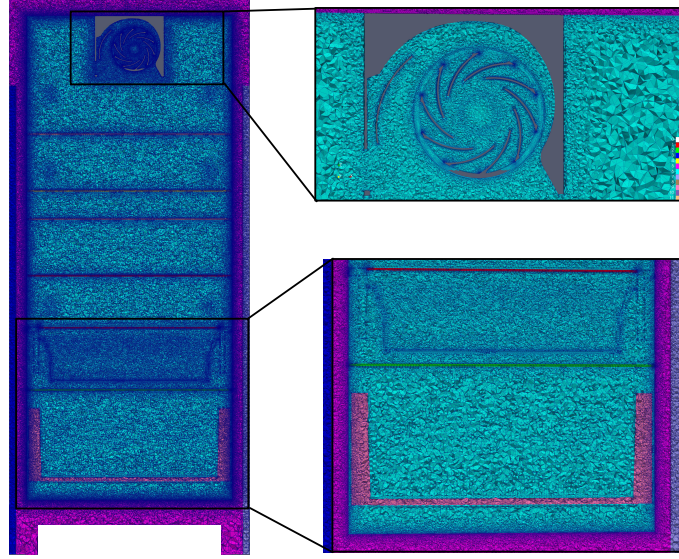


Figure 2: Mesh visualization: the figure displays the mesh of the computational domain. The two sub-panels provide a detailed view of the mesh in the fan region and the bottom part of the fridge.

it provides the flexibility to solve specific types of equations for each region and assign specific boundary conditions to different interfaces. The conformal mesh guarantees that there are no gaps or overlaps between regions which enables us to have a more accurate calculation of temperature and heat fluxes at the interface.

A sketch of the obtained multi-region mesh is illustrated in Fig. 2. The mesh consists of tetrahedral, hexahedral and polyhedral cells with the minimum and maximum mesh sizes of 0.1 mm and 32 mm, respectively, which results in a total of 20 millions of elements, approximately, for this geometry. Since the only equation to solve in solid components is the conduction equation, the mesh size is larger in these regions than the fluid region. The zoom-in sub-figures of Fig. 2 highlight the local refinements in the region of higher gradients such as near interface regions and fan. The refinement is essential to ensure that high gradients are accurately captured. The max non-orthogonality factor of the obtained mesh is less than 60 °, demonstrating that the resulting mesh is of good quality for CHT simulations.

The fan is modeled using the multiple reference frame (*MRF*) method [41]. This approach is a commonly used technique for fan modeling that provides a trade-off between accuracy and efficiency in simulations. In this approach, the fluid region is divided into two different regions: stationary and moving regions. *MRF* models the relative motion between the two regions by including a source term without actually moving the mesh.

4.1 Validation

To ensure the accuracy of our model, we validated the results of the CHT simulation against the experimental setup. For this purpose, two different fridge configurations were considered: static and ventilated fridges. In the static setup, the fan is inactive and the flow is driven by natural convection where buoyancy governs the fluid motion. On the other hand, in the ventilated configuration, the fan works with its maximum angular velocity $\omega = 191.6$ (rad/sec) resulting in forced convection. For both setups, we set the evaporator temperature (T_{evap}) to -15 °C and ambient temperatures (T_{amb}) to 32 °C. All the solid regions and air were initialized with the ambient temperature $T_{initial} = T_{amb} = 32$ °C to simulate a scenario where the fridge operates during warmer seasons. The steady-state temperature at the sensor points were recorded and compared against experimental measurements. To consider the thermal inertia of the solid in our study, we registered the temperature in the middle point of the cylindrical-shaped solid sensors rather than the cylinder surface which results in more accurate measurement.

Fig. 3 illustrates the locations of the sensors in the cabin and on the door of the fridge. The sensors located at the upper part of the fridge, with 5 sensors above each shelf, were named using two digits: the first digit indicates the level where the sensor is located, while the second one defines

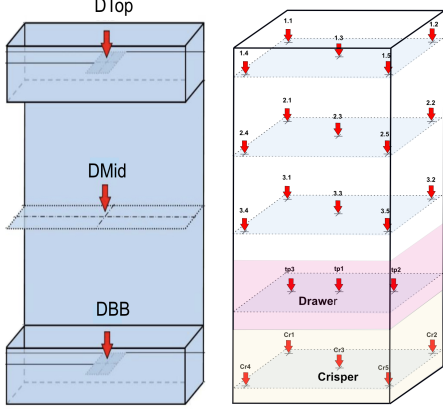


Figure 3: Sensor locations: The right panel illustrates the position of the sensor within the fridge cabin, while the sensor locations in the fridge door are shown in the left panel.

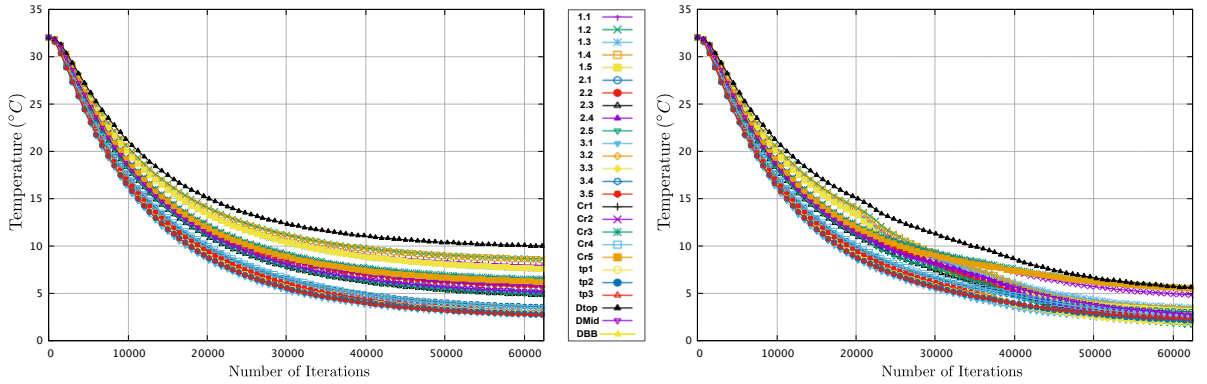


Figure 4: Steady state analysis: time evolution of the temperatures at sensor points. The left and right panels depict the temperature variation over time in the static and ventilated fridge setup, respectively.

the sensor number at that specific level. There are also 8 sensors in the bottom part of the fridge; 3 sensors in the drawer and 5 in the crisper. As the drawer volume is smaller than the crisper, fewer sensor numbers are used to monitor the temperature in the drawer. The locations of these 23 sensors are shown in the right panel of Fig. 3. Moreover, the left panel of Fig. 3 demonstrates the location of 3 sensors in the top, middle and bottom bins of the fridge door.

For both cases, we let the fluid flow evolves until the steady state in temperature was reached for the all sensors. The time evolution of temperature at the sensor points is depicted in Fig. 4 with the right and left panels showing the static and ventilated fridge configurations, respectively. Since both fridge configurations were initialized with the ambient temperature, all the sensors registered $T = 32^\circ\text{C}$ as the initial temperature. As the simulations progressed, the temperature at sensor points decreases due to the heat transfer in the fridge until stabilizing at a plateau. The static setup reached the stationary state after 50,000 iterations, while the achievement of steady-state was delayed for 5,000 more iterations in ventilated configuration due to the more complex dynamics of the fluid flow. We continued the simulation until 62,000 iterations in both cases to ensure the attainment of steady-state conditions.

For both cases, we observed that the highest temperature was recorded at the "Dtop" sensor, located at the top bin of the fridge door. We noticed that this temperature is lower in the ventilated case compared to the static setup, which aligns with our expectations. The reason is related to the enhanced mixing of the fluid flow caused by the presence of the fan. Consequently, the more uniform temperature distribution in the ventilated setup reduces temperature stratification between different levels of the fridge.

The comparisons of the steady-state temperature at the sensor points against experimental measurement were depicted in Fig. 5 with the right and left panels showing the validation in static

and ventilated fridge configurations, respectively. In both cases, the numerical data follow the same trend as the experiment. The maximum average temperature difference in both setups was observed at the sensors located on the first level of the fridge, $\Delta T_{avg} = 1.7 \text{ }^{\circ}\text{C}$ and $\Delta T_{avg} = 0.78 \text{ }^{\circ}\text{C}$ in static and ventilated configurations, respectively. The average temperature difference in the rest of the fridge is less than $1.5 \text{ }^{\circ}\text{C}$ which is an acceptable value for both cases.

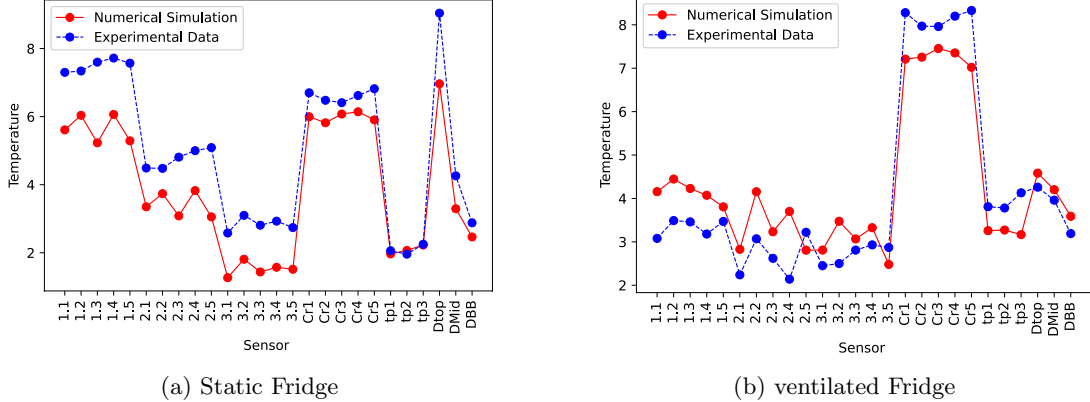


Figure 5: Validation of CHT model against experimental data. Left and right panels present the validation for static and ventilated fridge configurations, respectively.

The visual comparisons of velocity and temperature distribution on the side view for both static and ventilated configurations are presented in Fig. 6 and Fig. 7. In both figures, the left and right panels display the velocity and temperature distributions in the static and ventilated fridge, respectively. Fig. 7 clearly demonstrates that there is temperature stratification in the static fridge, where the upper region of the fridge is warmer than the lower part. Conversely, the ventilated fridge exhibits an improvement in temperature distribution; the temperature is more uniform and there is no significant temperature difference between the upper and lower parts of the fridge as a result of enhanced mixing. The velocity contours in Fig. 6 exhibit higher velocity magnitude and more turbulent structures in the fridge when the fan operates at its maximum velocity.

Following the validation of our CHT solver against the experimental data, the main purpose of this study is to develop a data-driven ROM for the fridge for which a comprehensive database needs to be collected. The database must include a wider range of data for specific parameters, known as "sensitive parameters". These parameters tend to change the system non-linearly and the system's response to their modification is more amplified. Consequently, it is crucial to increase the sampling density of these parameters to ensure that the dataset is tailored and comprehensive for each specific problem.

The ambient temperature, evaporator temperature and fan angular velocity are the parameters of interest in this study. To determine the most and least sensitive parameters, a sensitivity analysis was conducted for both fridge configurations by considering the most extreme values for each parameter: $T_{evap} = [-15, +4] \text{ }^{\circ}\text{C}$, $T_{amb} = [16, 32] \text{ }^{\circ}\text{C}$, and $\omega = [0, 191.6] \text{ rad/sec}$. These values are chosen based on the experimental tests. We carried out the simulations for the configurations, C_1 to C_8 , with combinations of parameters reported in Tab. 1.

Configuration	C_1	C_2	C_3	C_4	C_5	C_6	C_7	C_8
$T_{evap} (\text{ }^{\circ}\text{C})$	-15	-15	-15	-15	4	4	4	4
$T_{amb} (\text{ }^{\circ}\text{C})$	16	16	32	32	16	16	32	32
$\omega (\%)$	0	100	0	100	0	100	0	100

Table 1: Sensitivity analysis: simulation plan of various configurations to assess system sensitivity.

To analyze the system sensitivity with respect to the parameters, we computed the scatter matrix of temperature at the sensor points for the configurations listed in Tab. 1. The scatter matrix is a square matrix where the diagonal grids represent the variance of each configuration, while the off-diagonal grids indicate the covariance between pairs of configurations. Each point within the grids represents the relationship between a pair of temperatures at the same sensor.

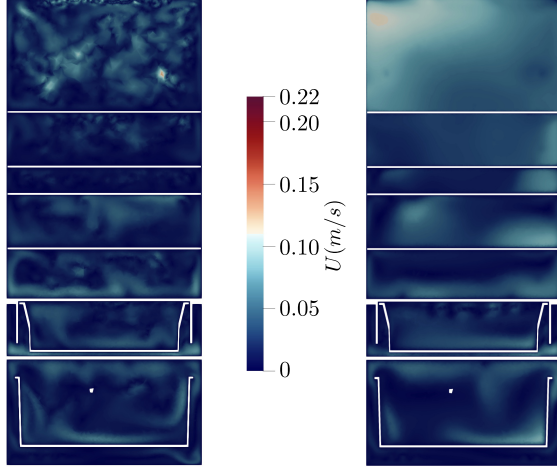


Figure 6: Velocity contour: visual comparison of the magnitude of velocity distribution in the static (left panel) and ventilated fridge, (right panel).

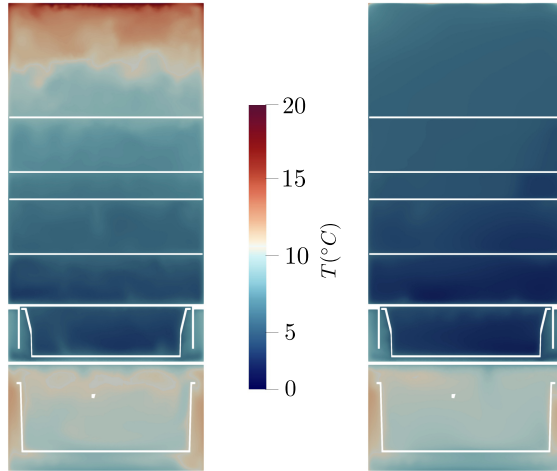


Figure 7: Temperature contour: visual comparison of temperature distribution in the static (left panel) and ventilated fridge, (right panel).

The distribution of the points within the grids defines the relationship among configurations. If the points follow a polynomial pattern of any order, there is a corresponding polynomial relationship between configurations. Conversely, the scattered points in a random pattern without any clear trend suggest a nonlinear relationship.

The results of this analysis are displayed in Fig. 8. We noticed a significant non-linear relationship when the fan velocity varies from 0 to 191.6 (rad/sec), as indicated by the covariance between C_1 and C_2 , as well as C_1 and C_6 configurations. On the other hand, changing the ambient and evaporator temperatures does not introduce non-linearity to the solution; the points mostly exhibit a linear correlation although some outliers are observed. Based on this analysis, we realized that fan velocity is the most sensitive parameter in our problem which requires a denser sampling. Consequently, 11 sampling points for this parameter were considered, ranging from $\omega_{min} = 0$ to $\omega_{max} = 191.6$ (rad/sec) with an increment of 10%. For the remaining parameters, 4 evaporator temperatures: $T_{evap} = [-15, -7.9, -3.25, +4]$ °C and 2 ambient temperatures: $T_{amb} = [16, 32]$ °C were considered. The combination of these parameters results in a total of 88 various configurations. A CHT simulation has been conducted for each configuration and the results were collected to build the database.

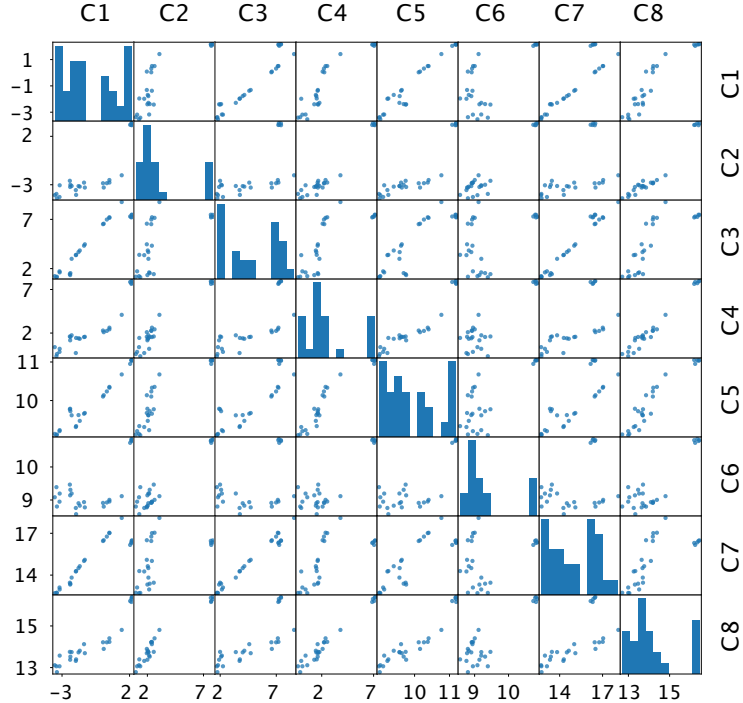


Figure 8: Sensitivity analysis: scatter matrix of temperature at sensor points for the configurations listed in Tab. 1. The diagonal elements represent the variance of each configuration, while the off-diagonal ones indicate the covariance between the two configurations.

5 Surrogate Model

Considering the computational expense of the high-fidelity numerical simulation, we develop reduced-order models to reconstruct the full temperature field at an unknown parameter value, where limited information (such as measurements at the sensor locations) or no information is available. First, we demonstrate the application of the POD-RBF method in Section 5.1 to reconstruct the temperature field at an unknown parameter value based on the solutions of the temperature field available at known parameter values. Next, we reconstruct the temperature field from a few sensor locations' temperature data (it can be both experimental or numerical, however, we considered numerical results for demonstration) using the conventional Gappy POD approach in Section 5.2. Finally, a stable deep learning-enhanced GPOD approach named ANNGPOD is employed in Section 5.3 and Section 5.4 to reconstruct the full temperature field provided sparse experimental and/or numerical datasets only at a few sensor locations. Figure 9 show 3 vertical and 8 horizontal planes where the temperature field is reconstructed. The horizontal planes are placed in such a way that they contain the sensor locations as shown in Fig. 3. To carry out the parametric study, the evaporator temperature T_{ev} , ambient temperature T_{amb} , and percentage of fan velocity, v_f are considered. As indicated in the previous section 4, from the sensitivity analysis, the training dataset density should be higher in the parametric direction of the fan velocity. Hence, the fan velocity ranges from 0 to 100 % of the full throttle which is 1600 rpm in step of 10 % i.e., total of 11, two ambient temperatures i.e., 16 °C and 32 °C, and 4 evaporator temperatures i.e., -15 °C, -7.9 °C, -3.25 °C and 4 °C are considered. Therefore, a total of 88 parametric locations are considered to generate high-fidelity simulation data. The total spatial size of the dataset combining the grid points of all the selected planes is 1443297. Therefore, the size of the input matrix is $\mathbb{R}^{(88 \times 3)}$ whereas the size of the output matrix is $\mathbb{R}^{(88 \times 1443297)}$ considering the total parametric locations, 88, type of parameters, 3 and total spatial location, 1443297. Now, in the following subsections, we demonstrate several reduced-order models of interest taking a part of the input dataset as training points and the rest parameter values as validation points.



Figure 9: Fridge Planes of interest for the temperature field reconstruction.

5.1 POD-RBF ROM

As mentioned earlier in the Section 3.1, the POD-RBF ROM consists of two stages: POD-based projection followed by the approximation using RBF interpolation. To minimize the prediction error using this ROM technique, the projection error must first be minimized. Singular Value Decomposition (SVD) is first applied to the dataset containing 88 parametric locations to compute the POD modes. Figure 10 shows cumulative energy or eigenvalues associated with the number of POD modes as shown in Eqn.16. With 3, 10, 25 and 58 modes, the system contains 99%, 99.5%, 99.7% and 99.9% of energy respectively.

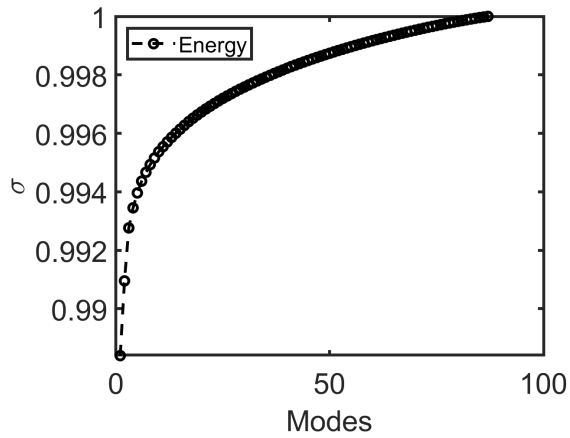


Figure 10: Cumulative energy with different number of modes associated with temperature field.

The temperature field is reconstructed at the mid-section, $x = 0$ considering different numbers of POD modes at a parametric point associated with T_{ev} of $-15\text{ }^{\circ}\text{C}$, T_{amb} of $16\text{ }^{\circ}\text{C}$ and v_f is kept at 100% as shown in Fig.11. At v_f of 100%, temperature field possesses significant non-linearity as compared to the condition when the fan velocity is less - therefore, this particular parametric point is chosen to assess the absolute error distribution when different numbers of POD modes are used for reconstruction. The absolute temperature error is computed as $|T_{CFD} - T_{ROM}|$, where

the T_{CFD} is the high-fidelity temperature field and the T_{ROM} is the temperature field associated with the surrogate model computed at the vertex centres ($n = 1443297$) of the computational cells contained in the 11 planes of interest. It is noticed, at $\sigma = 0.99$, the maximum error related to it is $3.17 \text{ }^{\circ}\text{C}$. The maximum temperature error occurred at the top-left corner of the section due to possible stagnation points and absolute temperature rise. However, the non-linearity of the flow physics is increased inside the crisper (lowermost chamber of the fridge) due to the generation of a flow vortex, as the air inside the fridge gets swept away by the fan situated at the top of the fridge, which eventually raises the temperature prediction error. However, at $\sigma = 0.995$, $\sigma = 0.997$, $\sigma = 0.999$ the maximum error associated with it is $1.68 \text{ }^{\circ}\text{C}$, $0.97 \text{ }^{\circ}\text{C}$ and $0.18 \text{ }^{\circ}\text{C}$. With $\sigma = 0.997$ and $\sigma = 0.999$, the projection-error distribution is less than 0.25 K throughout the sections. The temperature error distribution is significantly low for the other 10 sections when the number of modes is considered more than 25 and σ is higher or equal to 0.997.

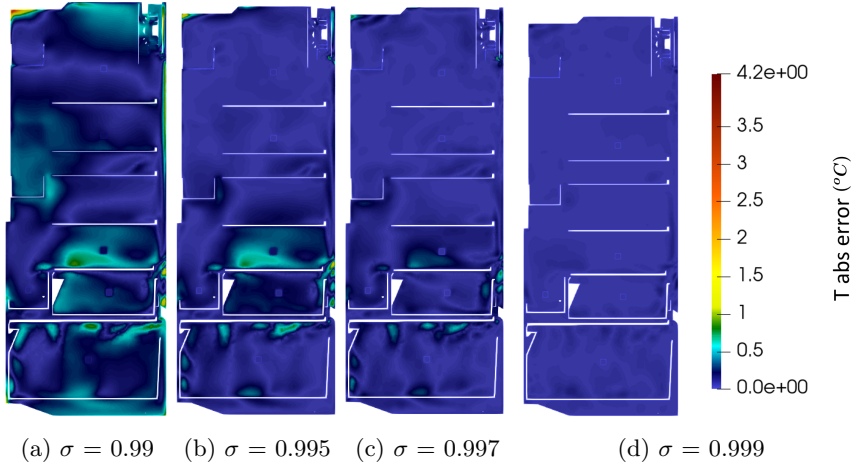


Figure 11: POD-based reconstruction error associated with the temperature field of the mid-section at $x = 0$

Now, to employ POD-RBF ROM, We aim to reconstruct the temperature field corresponding to a particular parameter value while the rest 87 parametric points are considered to be training points, the reduced coefficient obtained from the temperature fields associated with the training parameter values are interpolated using the RBF approach to reconstruct the temperature field associated with an unknown parameter of interest. Fig.12, shows the absolute temperature error distribution at different planes corresponding to $T_{amb} = 16 \text{ }^{\circ}\text{C}$, $T_{ev} = -15 \text{ }^{\circ}\text{C}$, and $f_v = 100\%$. However other than a few locations such as the start of any narrow passages, where the velocity drops due to stagnation, temperature increases thereby increasing the absolute temperature error as well, the majority of the spatial locations show an error distribution less than $0.5 \text{ }^{\circ}\text{C}$.

Next, considering the computationally expensive full-order simulation, we aim to reduce the computation effort required to generate the dictionary of the training dataset by sparsifying the number of training points to produce accurate ROM. Previously in Fig.12, the size of training parametric points is 87 (99% of the total input size), but now we will consider 85%, 48%, 30% and 13% of the total input size. Figure 13 shows prediction error associated with different percentages of data. The parameter values outside the training datasets are considered as the validation points. Therefore, 15%, 52%, 70% and 87% corresponding to the above-mentioned training sets are available for validation. The average (MAE_{avg}) and the maximum (MAE_{max}) over all the validation points' mean absolute error (MAE) are computed as shown in Eqn 33:

$$\begin{aligned} MAE_{avg} &= \frac{1}{n_{val}} \left(\sum_{n_{val}} \left(\frac{1}{n_{planes}} \sum_{n_{planes}} |(T_{CFD} - T_{ROM})| \right) \right) \\ MAE_{max} &= \max_{n_{val}} \left(\frac{1}{n_{planes}} \sum_{n_{planes}} |(T_{CFD} - T_{ROM})| \right) \end{aligned} \quad (33)$$

where n_{planes} and n_{val} are the total number of planes of interest inside the fridge and validation points. The MAE_{avg} and MAE_{max} associated with the validation points are shown in Fig.13. The

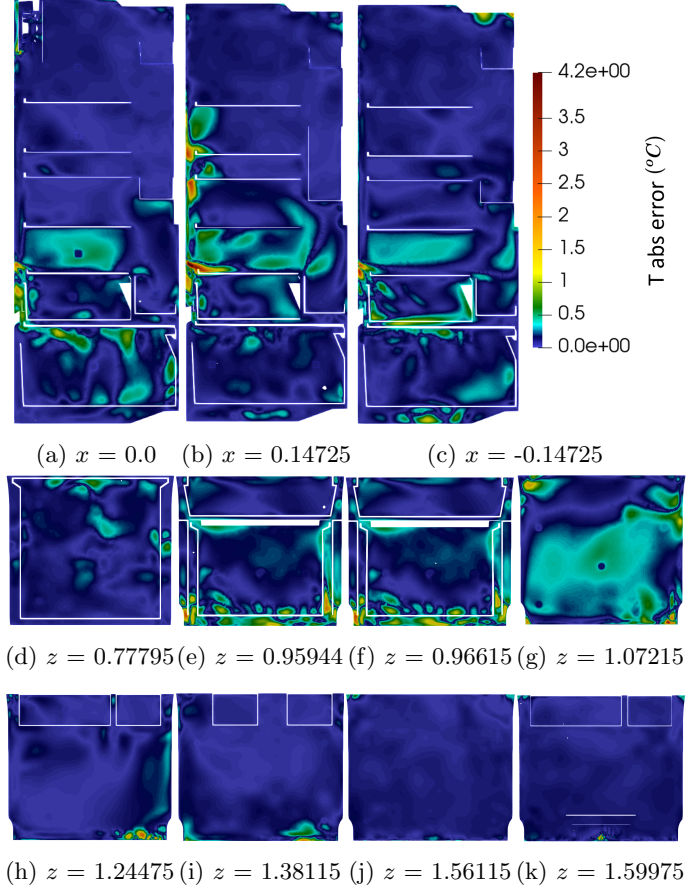


Figure 12: Reconstruction error associated with the temperature field using POD-RBF method

dotted line indicates the MAE_{avg} whereas the upper bound of the graph shows the MAE_{max} corresponding to different percentages of the training datasets considered. It is evident from 13a and 13b, when the training data size is large which is 85%, MAE_{avg} is minimum at most of the planes except for planes no. 1, 7, 8. However the improvement of the MAE_{avg} and MAE_{max} is not linear with the enrichment of the training dataset. When the training dataset size is 13 %, the MAE_{avg} is maximum at all the planes. The MAE_{max} , similarly shows minimum prediction accuracy at 13 % of the training data, whereas maximum prediction accuracy at the most dense dataset considering the majority of the planes. The MAE_{avg} for all the training sets lies around $0.25 \text{ }^{\circ}\text{C}$ whereas the MAE_{max} does not cross the error limit of $1 \text{ }^{\circ}\text{C}$ even at most sparse training dataset.

5.2 Gappy POD

In this current section, the temperature field is reconstructed using the temperature measurements at a few sensor locations [54]. As discussed in section 3.3, for the application of Gappy POD, apart from the training datasets where high-fidelity results are available, a sparse temperature dataset is also available at all or a few locations of the 26 sensors shown in Fig. 3 corresponding to validation parameter values. If the number of sensors and the number of POD modes are different, Φ_R matrix in Eqn. 28 is rectangular. To avoid the computation of the pseudo-inverse (\dagger) of the truncated Φ matrix (Φ_R) and additional prediction error as a result of it, we have maintained the number of modes equal to the number of sensor locations. Furthermore, the prediction accuracy associated with the conventional Gappy POD is very sensitive to the location and number of the sensors. In this section, we will show the absolute and mean temperature field reconstruction error associated with different planes of interest considering only the 5 mid-sensor locations as indicated by 1.3, 2.3, 3.3, *tp1* and *cr3* in Fig. 3. Figure 14 shows that using the Gappy-POD approach, the error associated with the 11 planes is higher compared to the POD-RBF approach.

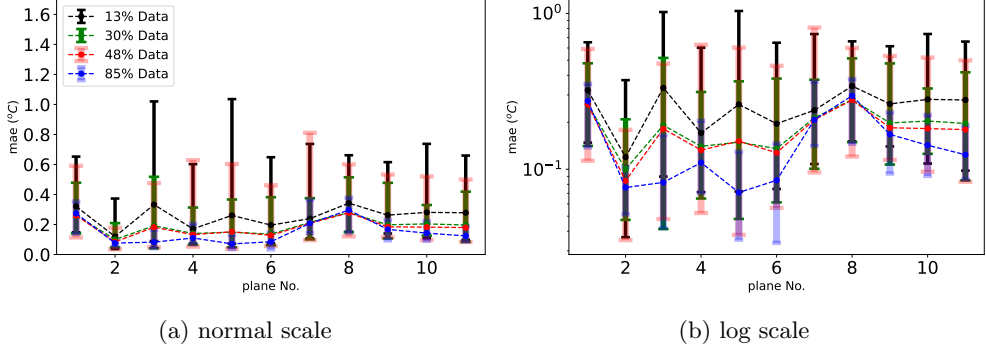


Figure 13: Mean absolute error associated with the prediction of POD-RBF ROM with benchmark CFD data using different percentages of training datasets.

Here, we have considered the parametric location corresponding to $T_{amb} = 16^\circ C$, $T_{ev} = -15^\circ C$, and $f_v = 100\%$ for the validation and the rest 87 parameters are training points. At sections, $z = 0.95944$, $z = 0.96615$ and $z = 1.07215$ the absolute error distribution crosses the error limit of $1^\circ C$ at majority of the spatial locations. In the following section 5.3, we will show that with different numbers of sensor locations, the performance of the conventional GPOD further deteriorates, whereas our proposed ANNGPOD outperforms the classical method.

Similar to the previous section 5.1, we now aim to reduce the training points to minimise the computational effort associated with the training dataset generation. Although, the MAE_{avg} associated with 30%, 48% and 85% training data is around $0.5^\circ C$, the MAE_{max} crosses the error limit of $1^\circ C$, when the training points are sparsified beyond 48%. Additionally, we observe that the GPOD ROM with 48% dataset shows poor performances as compared to the one with even sparse datasets, i.e., 30% training datasets at most of the planes.

5.3 Deep-learning enhanced Gappy POD

In this subsection, the deep-learning enhanced gappy-POD approach as shown in section 3.4 is demonstrated for the temperature field reconstruction at parameter values corresponding to validation points. In the case of the GPOD approach, the number of modes is kept equal to the number of sensor locations. Conversely, there are no similar constraints on the ANNGPOD method, since Eqn. 32 is solved using an optimization framework in the ANN network. Therefore the number of modes is decided in the ANNGPOD method based on how much energy of the dynamical system, the reduced order system must contain, such as 99.7 % in the present case scenario. The number of sensor locations can be chosen independently of the number of modes considered. Fig. 16 compares the MAE using GPOD and ANNGPOD methods while considering 87 training points and 1 validation point. Sparse temperature solutions at a few sensor locations are available at the validation parametric point. 4 different numbers of sensor locations i.e., 5, 15, 20 and 26 are considered. In our current assessment of the mean absolute projection error at different planes, we will mainly focus on 3 different parameters varying the T_{amb} , T_{ev} , and v_f i.e., $p = 10$ corresponds to $T_{amb} = 16^\circ C$, $T_{ev} = -15^\circ C$, and $v_f = 100\%$; $p = 22$ corresponds to $T_{amb} = 16^\circ C$, $T_{ev} = -7.9^\circ C$, and $v_f = 0\%$ and $p = 62$ corresponds to $T_{amb} = 32^\circ C$, $T_{ev} = -3.25^\circ C$, and $v_f = 70\%$. In Fig. 16a and Fig. 16b, $p = 10$, v_f of 100 % introduces strong non-linearity in the flowfield. With 26 and 20 sensors, the prediction accuracy associated with the conventional GPOD method is poor as the MAE is above $1^\circ C$ at all planes. Conversely, with the ANNGPOD method, the MAE is within the acceptable limit for all the number of sensor locations. In the previous sub-section 5.2, the application of the GPOD approach in absolute error distribution is demonstrated with 5 sensor locations. From Fig. 16b, it is observed that prediction accuracy with 5 sensors using the ANNGPOD method is better than the GPOD method with 5 sensors at most of the planes except for the plane 7. Although ANNGPOD does not show linear improvement in the prediction accuracy with the increase in the number of sensors, with sensors' numbers of 26 and 20, the MAE error is much less than the ones associated with sensors' no. of 5 and 15. Conversely, the conventional GPOD does not show any correlation between the prediction accuracy with the number of sensors. It justifies the stability of our new approach ANNGPOD as compared to the classical GPOD

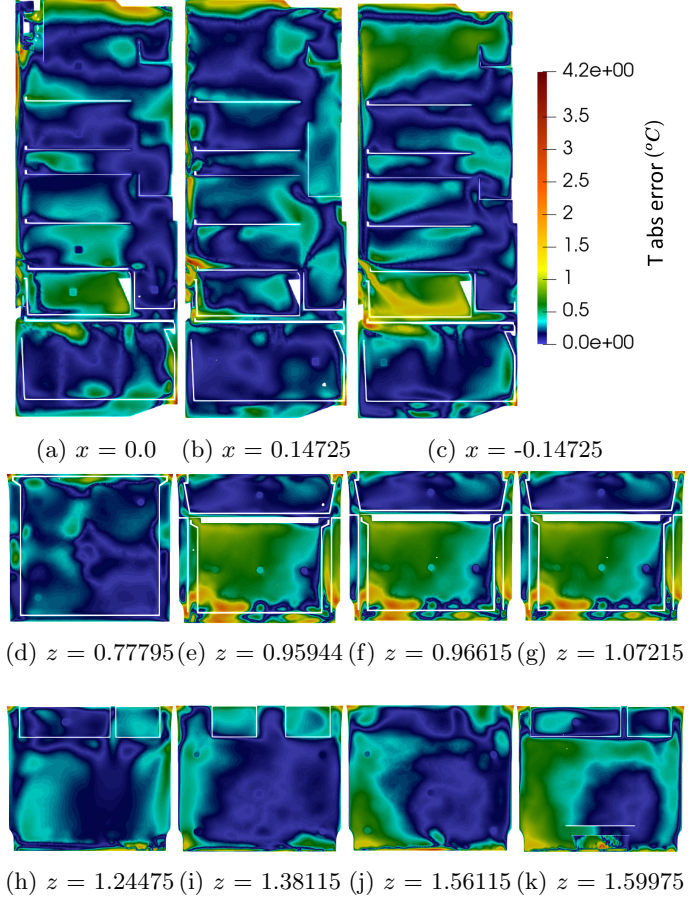


Figure 14: Reconstruction error associated with the temperature field using Gappy POD approach.

method. In Fig. 16e and Fig. 16f, nonlinear convection is reduced as the v_f is 70%. GPOD with 26 sensors is the only outlier among all the sensors' numbers variations using GPOD and ANNGPOD methods. On the contrary, in Fig. 16c and Fig. 16d, v_f is 0, that means the non-linearity of the flow physics is greatly reduced and only contributed by natural convection term. Here, both the GPOD and ANNGPOD method produces prediction errors within an acceptable limit of 1 °C. However, with $p = 22$ and $p = 62$, the ANNGPOD prediction with 20 and 26 sensors is better than the other variations of sensor numbers similar to what was observed in the case of $p = 10$. For the development of the ANNGPOD method, the POD-ANN approach is considered. In the ANN, 2 intermediate hidden layers with 200 and 64 neurons are considered. The activation functions are *ReLU*, *Tanh* and *Tanh* associated with the hidden layers and the output respectively. A learning rate of 0.01 with a decay rate of 0.75 in step-size of 1000 is considered. The number of epochs is chosen as 20000.

Fig. 17 shows the distribution of the absolute error in the middle plane, indicated as plane 11 in Fig. 9 while using sparse temperature data at 26 sensor locations. The parametric location $p = 10$ is considered for this application. This analysis also demonstrates that the ANNGPOD always produces stable solutions whereas the conventional GPOD-based prediction can be completely erroneous as shown in Fig. 17b based on the number or location of the sensors chosen. We also show the absolute error distribution at all the planes corresponding to $p = 10$ and using 26 sensor locations in Fig. 18. However, the error distribution is comparable to the one demonstrated by the GPOD method using 5 sensors and shown in Fig. 14, the potential of the ANNGPOD method lies in producing stable reconstruction at any number or locations of the sensors. Furthermore, the hyper-parameters of the ANN network can be tuned to improve the prediction accuracy which is not possible in the case of the conventional GPOD method. Additionally, the weights mentioned in Eqn. 32, can also be varied to improve the prediction accuracy i.e., λ_1 and λ_2 can be used to decide the amount of information or feedback necessary to be considered from the numerical datasets available at training parameters or from the numerical or experimental sparse dataset

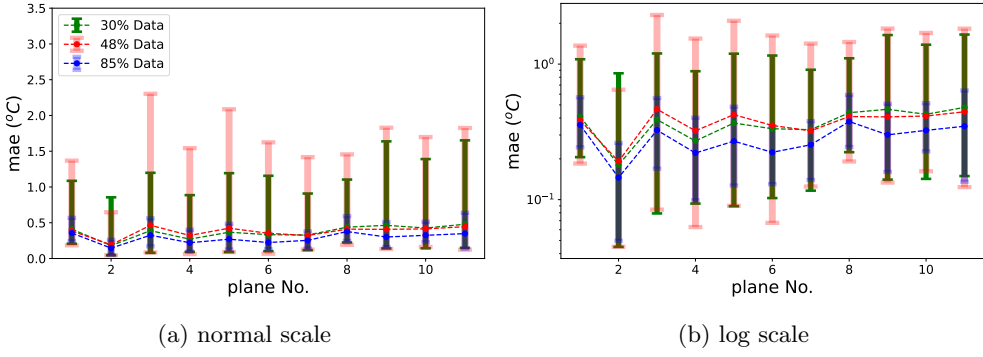


Figure 15: Mean absolute error associated with the prediction of Gappy POD-based ROM with benchmark CFD data using different percentages of training datasets.

available at the sensor locations of validation parameters while predicting the full temperature field at all the spatial grid locations corresponding to the validation parameters' values.

Next, we consider sparse training datasets and compare the predicted results at all the validation points. It shows that with the usage of 5 and 26 sensors, the MAE_{avg} and MAE_{max} is less than 1°C . For prediction using 26 sensors and ANNGPOD method, 2 inner layers with 200 and 64 neurons are considered. Furthermore, for the 5 sensors, 20 neuron with one single layer is considered. With 85% case, the prediction error in terms of MAE_{avg} and MAE_{max} is minimum, and with sparsifying the training dataset, the prediction error increases. However, the prediction improvement is not monotonic with the increment in the training dataset, such as with the 48% data, the ANNGPOD method has shown poor performance than the 13% and 30% training data at most of the planes while using the number of sensors 5 in Fig. 19b and 26 in Fig. 19d respectively.

5.4 ANNGPOD with Experimental Sensor Data

We have considered the experimental result available for the parameter value T_{ev} of -15°C , T_{amb} of 32°C , v_f of 0%. Out of 26 experimental sensors data available as shown in Fig. 3, we have considered only the middle sensors' datasets i.e., 1.3, 2.3, 3.3, *tp1* and *cr3* as an input in ANNGPOD method. The temperature prediction is validated at 26 sensor locations where the experimental dataset is available. We have compared the prediction at the 26 points with CFD and the experiments when 13 % and 98 % training high-fidelity datasets are used respectively as shown in Fig. 20. Table 2 shows the mean absolute error of the predicted temperature using ANNGPOD and POD-RBF at the 26 sensor points with respect to the experiments and high-fidelity CFD results. As shown in Fig. 20 and Table 2, the POD-RBF ROM produces a mean absolute error of 0.3532 and 0.5725 using 98% and 13% CFD data when compared with the high-fidelity CFD simulation at the unknown parameter value. However, the prediction error with respect to experimental data at 26 sensor locations is significantly higher, 1.0273°C and 1.2562°C . The POD-RBF-based prediction is completely based on the high-fidelity simulation data and does not receive any feedback from experimental results therefore, the surrogate model prediction moves away from the experimental results. As shown in Fig. 20a and Fig. 20b, the high-fidelity results are always below the experimental results at all the 26 sensor locations. The RBF-POD ROM pushes the temperature prediction further down which results in a large mean absolute error with respect to the experiments. Conversely, in the ANNGPOD method, the prediction from the surrogate model takes 5 sensors' temperature data as input from experiments and therefore reducing the mean absolute prediction error to 0.5925°C and 0.4960°C while using 98% and 13% numerical simulation data as training dataset. This is also important to note that when the 13% numerical simulation data is considered as a training dataset, the prediction error of the surrogate model with respect to the experimental results is lower as compared to the one reported for the 98% training dataset. Since the ANNGPOD method is based on the minimization of loss terms derived from the numerical training dataset and experimental inputs, the later part (experimental) gets additional weightage when 13% numerical CFD dataset is used.

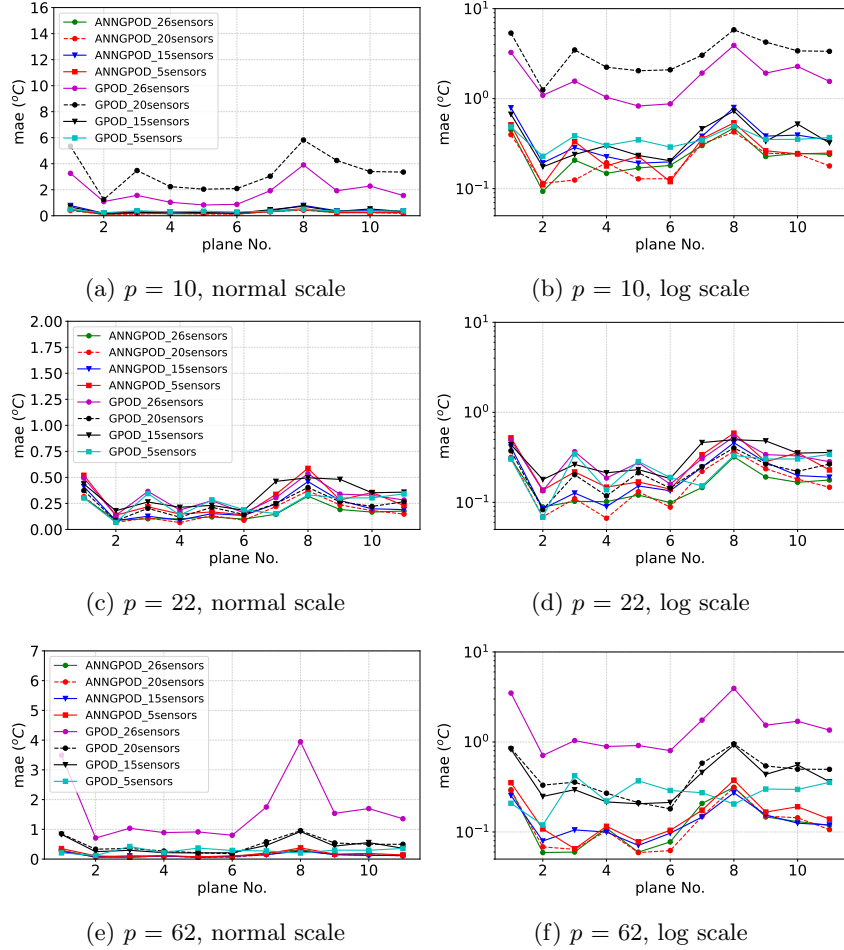


Figure 16: Mean absolute error of temperature field prediction associated with different planes of interest using Gappy POD and ANNGPOD approach.

Average Error over 26 pts (in K)	POD-RBF (98 %)	ANNGPOD (98 %)
ROM vs CFD	0.3532	0.2310
Exp vs CFD	0.6837	0.6837
ROM vs Exp	1.0273	0.5925
Average Error over 26 pts (in K)	POD-RBF (11 %)	ANNGPOD (11 %)
ROM vs CFD	0.5725	1.0253
Exp vs CFD	0.6837	0.6837
ROM vs Exp	1.2562	0.4960

Table 2: prediction accuracy of ANNGPOD method with respect to the experimental results at 5 mid sensors

5.5 Computational cost

We briefly discuss the efficiency of our ROM approach. The FOM simulations were carried out on a supercomputer using 128 processes. The computing nodes were equipped with Xeon E5-2683 v4 processors (2 sockets, 32 cores) and 64GB RAM. The CPU time associated with the FOM simulation is around 1e6 s. The ROM simulations were conducted on an 11th Gen Intel(R) Core(TM) i7-11700 @ 2.50GHz 32GB RAM by using one only processor. The training time associated with the POD-RBF ROM is 35.24 s while the prediction time at all the 11 planes of interest is 0.64 s. Conversely, in the case of ANNGPOD ROM, there are no distinctions between the training and prediction phases, for each unknown parameter value we need to rerun the algorithm for the reconstruction of the temperature field. Therefore the approximate time taken for the ANNGPOD

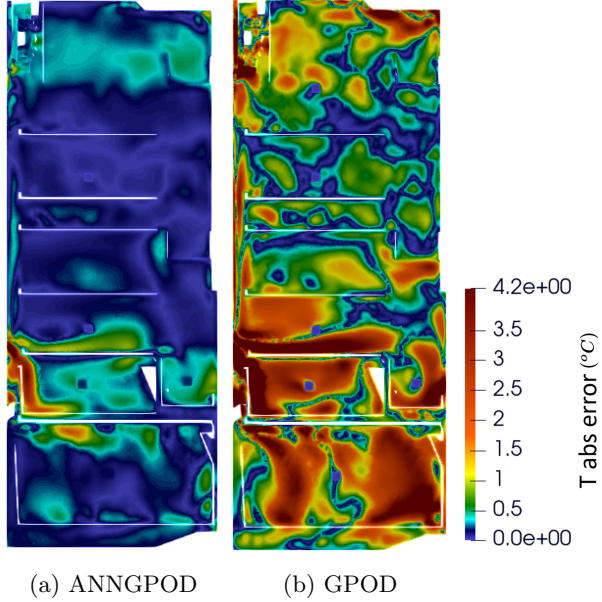


Figure 17: Absolute error considering ANNGPOD and conventional Gappy POD with 26 sensors at the ($x = 0$) plane.

prediction is 193.01 s . It is evident from the computational cost associated with the POD-RBF and ANNGPOD ROM that, the POD-RBF ROM can be used for the real-time analysis while the latter can not be used which is the limitation of our present approach. However, a significant computational speed-up is achieved, i.e., for POD-RBF ROM, it is $1\text{e}6$ and for ANNGPOD it is $5\text{e}3$ times.

6 Concluding remarks

In This study, the thermal behaviour of a household fridge was investigated through Conjugate Heat Transfer (CHT) simulation. To ensure the accuracy and reliability of the suggested model, it was validated against experimental setup for two various configurations: static and ventilated fridges. Moreover, we conducted a sensitivity analysis for the key parameters of this problem. The result identified that creating a tailored database for this problem requires denser sampling of the fan velocity, as the most sensitive parameter. This database forms the foundation for the development of a non-intrusive data-driven Reduced Order Model (ROM) for the fridge. In this work, we propose two different types of ROM: POD-RBF and ANNGPOD methods for the exploration of the parametric space - the former considers only high-fidelity numerical data as a training dataset while the latter can use both experimental and numerical data for the temperature field prediction at 11 planes of interest. We have shown that the POD-RBF ROM produces a mean absolute error of less than $1\text{ }^{\circ}\text{C}$ with respect to the high-fidelity simulation results at all 11 planes while using a very sparse training dataset of 11 %. We have proposed a novel parametric ROM ANNGPOD capable of taking both experimental and numerical data as inputs. It outperforms the conventional Gappy POD approach producing a very accurate prediction error below the limit of 1 K at very sparse datasets and at any number of sensors while the classical Gappy POD produces accurate prediction only when a selected number of sensors are considered using a relatively richer training dataset. While carrying out this comparison we have solely considered the numerical datasets for both methods. Finally, the experimental datasets are considered at 5 sensor locations as input alongside the numerical training dataset at selected training parameter values and we have demonstrated that the ANNGPOD produced very accurate predictions close to the experiments at 26 sensor locations as compared to the POD-RBF ROM which does not take any feedback from the experiments and thereby demonstrating the potential of our novel approach, ANNGPOD. Looking ahead, recent advances in hybrid deep-learning architectures, such as [24], highlight promising directions for further enhancing the predictive capability of ROMs in CHT problems.

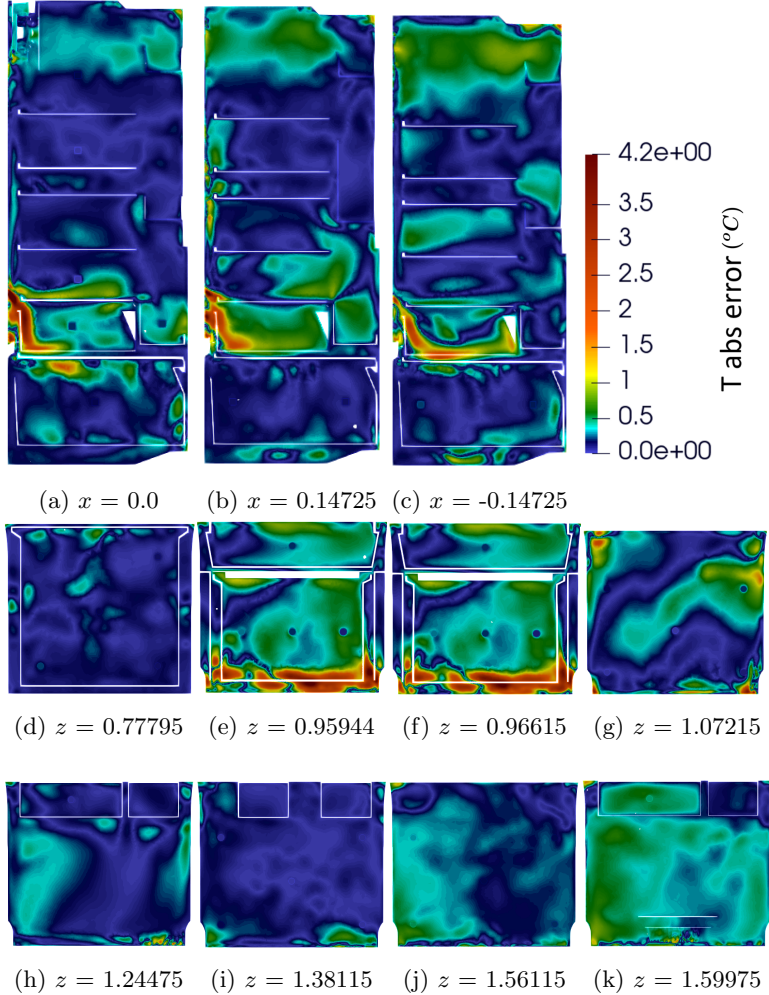


Figure 18: Reconstruction error associated with the temperature field using the proposed ANNG-POD approach with 26 sensors.

7 acknowledgments

We acknowledge the support provided by the European Research Council Executive Agency by the Consolidator Grant project AROMA-CFD "Advanced Reduced Order Methods with Applications in Computational Fluid Dynamics" - GA 681447, H2020-ERC CoG 2015 AROMA-CFD, the European Union's Horizon 2020 research and innovation program under the Marie Skłodowska-Curie Actions, grant agreement 872442 (ARIA), PON "Research and Innovation on Green related issues" FSE REACT-EU 2021 project, PRIN NA FROM-PDEs project, INdAM-GNCS 2019-2021 projects. We also would like to acknowledge Electrolux Company for their valuable support and fruitful discussion. Their expertise and assistance greatly contributed to the success of this research.

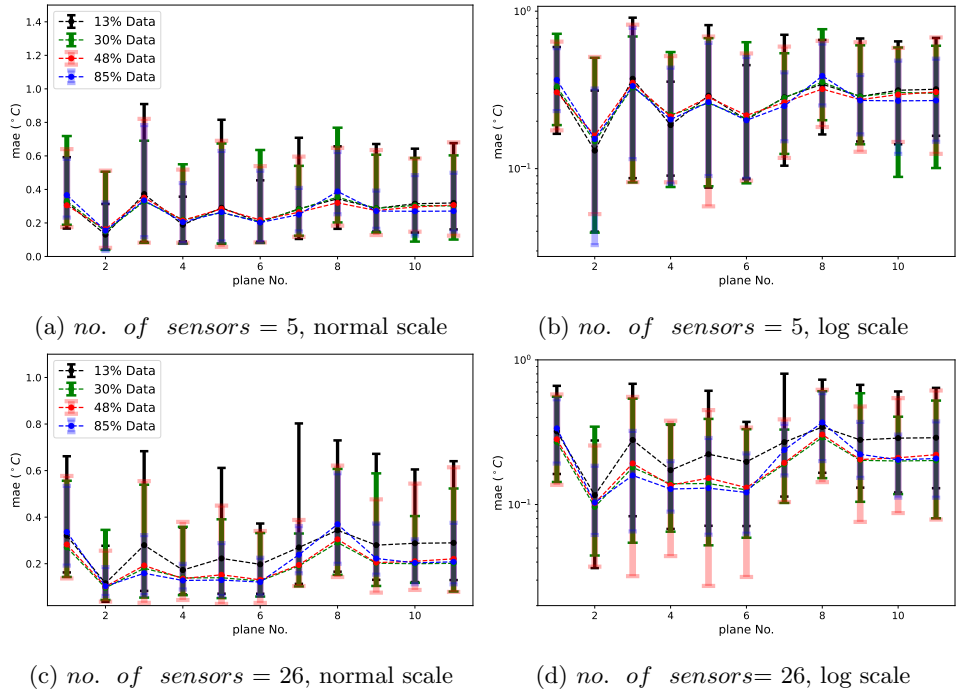


Figure 19: Mean absolute error associated with the temperature field prediction using Gappy POD and ANNGPOD approach considering available data (numerical) at 5 and 26 sensor locations, respectively.

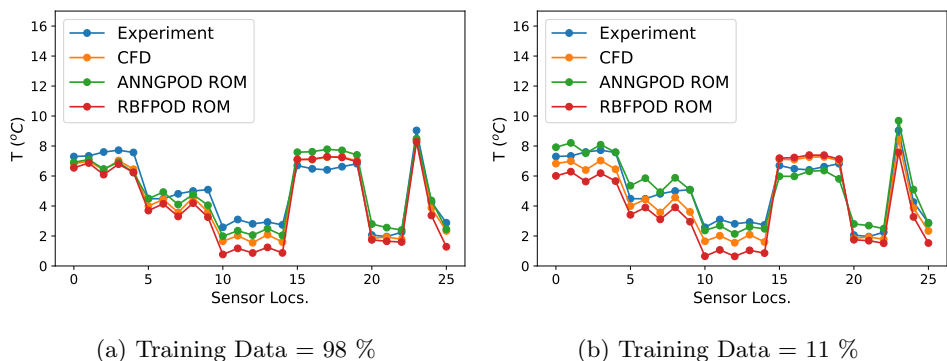


Figure 20: Temperature prediction using the ANNGPOD method with available experimental data at 5 sensors' locations.

References

- [1] Kabir Bakhshaei, Hoomaan MoradiMaryamnegari, Sadjad SalavatiDezfouli, Abdol Majid Khoshnood, and Mani Fathali. Multi-physics simulation of an insect with flapping wings. *Proceedings of the Institution of Mechanical Engineers, Part G: Journal of Aerospace Engineering*, 235(10):1318–1339, 2021.
- [2] Kabir Bakhshaei, Umberto Emil Morelli, Giovanni Stabile, and Gianluigi Rozza. Optimized bayesian framework for inverse heat transfer problems using reduced order methods. *arXiv preprint arXiv:2402.19381*, 2024.
- [3] Kabir Bakhshaei, Sajad Salavatidezfouli, Giovanni Stabile, and Gianluigi Rozza. Stochastic parameter prediction in cardiovascular problems. *arXiv preprint arXiv:2411.18089*, 2024.
- [4] C. Balaji and S.P. Venkateshan. Correlations for free convection and surface radiation in a square cavity. *International Journal of Heat and Fluid Flow*, 15(3):249–251, 1994.
- [5] C. Balzotti, P. Siena, M. Girfoglio, A. Quaini, and G. Rozza. A data-driven Reduced Order Method for parametric optimal blood flow control: application to coronary bypass graft. *Communications in Optimization Theory*, 26:1–19, 2022.
- [6] O. Bayer, R. Oskay, A. Paksoy, and S. Aradag. CFD simulations and reduced order modeling of a refrigerator compartment including radiation effects. *Energy conversion and management*, 69:68–76, 2013.
- [7] R. Ben-Mansour, A. Abuelyamen, and Esmail M.A. Mokheimer. CFD analysis of radiation impact on stirling engine performance. *Energy conversion and management*, 152:354–365, 2017.
- [8] M. D. Buhmann. Radial basis functions. *Acta numerica*, 9:1–38, 2000.
- [9] T. Bui-Thanh, M. Damodaran, and K. Willcox. Aerodynamic data reconstruction and inverse design using proper orthogonal decomposition. *AIAA journal*, 42(8):1505–1516, 2004.
- [10] P. J. Burns and D. V. Pryor. Surface radiative transport at large scale via monte carlo. *Annual Review of Heat Transfer*, 9, 1998.
- [11] D. Büschgens, C. Schubert, and H. Pfeifer. Radiation modelling of arbitrary two-dimensional surfaces using the surface-to-surface approach extended with a blocking algorithm. *Heat and Mass Transfer*, 58(9):1637–1648, 2022.
- [12] Wesley J Cole, Kody M Powell, Elaine T Hale, and Thomas F Edgar. Reduced-order residential home modeling for model predictive control. *Energy and Buildings*, 74:69–77, 2014.
- [13] N. Demo, M. Tezzele, G. Gustin, G. Lavini, and G. Rozza. Shape optimization by means of proper orthogonal decomposition and dynamic mode decomposition. *Technology and Science for the Ships of the Future: Proceedings of NAV 2018: 19th International Conference on Ship & Maritime Research*, page 212–219, 2018.
- [14] N. Demo, M. Tezzele, A. Mola, and G. Rozza. A complete data-driven framework for the efficient solution of parametric shape design and optimisation in naval engineering problems. *arXiv preprint arXiv:1905.05982*, 2019.
- [15] Nicola Demo, Marco Tezzele, Gianluca Gustin, Gianpiero Lavini, and Gianluigi Rozza. Shape optimization by means of proper orthogonal decomposition and dynamic mode decomposition. In *Technology and Science for the Ships of the Future*, pages 212–219. IOS Press, 2018.
- [16] Nicola Demo, Marco Tezzele, Andrea Mola, and Gianluigi Rozza. An efficient shape parametrisation by free-form deformation enhanced by active subspace for hull hydrodynamic ship design problems in open source environment. *arXiv preprint arXiv:1801.06369*, 2018.
- [17] R. Everson and L. Sirovich. Karhunen–loeve procedure for gappy data. *JOSA A*, 12(8):1657–1664, 1995.

- [18] T. L. Fine. *Feedforward neural network methodology*. Springer Science & Business Media, 1999.
- [19] A. Frank, W. Heidemann, and K. Spindler. Modeling of the surface-to-surface radiation exchange using a monte carlo method. In *Journal of Physics: Conference Series*, volume 745, page 032143. IOP Publishing, 2016.
- [20] M. Girfoglio, F. Ballarin, G. Infantino, F. Nicoló, A. Montalto, G. Rozza, R. Scrofani, M. Comisso, and F. Musumeci. Non-intrusive podi-rom for patient-specific aortic blood flow in presence of a lvad device. *Medical Engineering & Physics*, 107:103849, 2022.
- [21] D. M. Godino, S. F. Corzo, and D. E. Ramajo. CFD simulation of conjugated heat transfer with full boiling in openfoam (r). *Applied Thermal Engineering*, 213:118627, 2022.
- [22] H. Gunes, S. Sirisup, and G. Em. Karniadakis. Gappy data: To krig or not to krig? *Journal of Computational Physics*, 212(1):358–382, 2006.
- [23] Arash Hajisharifi, Michele Girfoglio, Annalisa Quaini, and Gianluigi Rozza. A comparison of data-driven reduced order models for the simulation of mesoscale atmospheric flow. *Finite Elements in Analysis and Design*, 228:104050, 2024.
- [24] Arash Hajisharifi, Michele Girfoglio, Annalisa Quaini, and Gianluigi Rozza. Combining extended convolutional autoencoders and reservoir computing for accurate reduced-order predictions of atmospheric flows. *arXiv preprint arXiv:2504.01097*, 2025.
- [25] Arash Hajisharifi, Rahul Halder, Michele Girfoglio, Andrea Beccari, Domenico Bonanni, and Gianluigi Rozza. An lstm-enhanced surrogate model to simulate the dynamics of particle-laden fluid systems. *Computers & Fluids*, 280:106361, 2024.
- [26] Arash Hajisharifi, Francesco Romano, Michele Girfoglio, Andrea Beccari, Domenico Bonanni, and Gianluigi Rozza. A non-intrusive data-driven reduced order model for parametrized cfd-dem numerical simulations. *Journal of Computational Physics*, 491:112355, 2023.
- [27] F. P. Incropera, D. P. DeWitt, Lavine Bergman, T. L., A. S., et al. *Fundamentals of heat and mass transfer*, volume 6. Wiley New York, 1996.
- [28] A. Kaplan, M. A. Cane, Y. Kushnir, A. C. Clement, M. B. Blumenthal, and B. Rajagopalan. Analyses of global sea surface temperature 1856–1991. *Journal of Geophysical Research: Oceans*, 103(C9):18567–18589, 1998.
- [29] D. Kim and J. Kim. Simulation of a conjugate heat transfer using a precice coupling library. In *Transactions of the Korean nuclear society virtual spring meeting, July 9*, volume 10, page 2020, 2020.
- [30] O. Laguerre, S. B. Amara, J. Moureh, and D. Flick. Numerical simulation of air flow and heat transfer in domestic refrigerators. *Journal of food engineering*, 81(1):144–156, 2007.
- [31] O. Laguerre and D. Flick. Heat transfer by natural convection in domestic refrigerators. *Journal of food engineering*, 62(1):79–88, 2004.
- [32] D. Lahaye, P. Nakate, K. Vuik, F. Juretić, and M. Talice. Modeling conjugate heat transfer in an anode baking furnace using openfoam. *Fluids*, 7(4):124, 2022.
- [33] A. Laitinen, K. Saari, K. Kukko, P. Peltonen, E. Laurila, J. Partanen, and V. Vuorinen. A computational fluid dynamics study by conjugate heat transfer in openfoam: A liquid cooling concept for high power electronics. *International Journal of Heat and Fluid Flow*, 85:108654, 2020.
- [34] N. C. Markatos and K.A. Pericleous. Laminar and turbulent natural convection in an enclosed cavity. *International journal of heat and mass transfer*, 27(5):755–772, 1984.
- [35] S. Mazumder. Application of a variance reduction technique to surface-to-surface monte carlo radiation exchange calculations. *International Journal of Heat and Mass Transfer*, 131:424–431, 2019.

- [36] F. R. Menter. Two-equation eddy-viscosity turbulence models for engineering applications. *AIAA journal*, 32(8):1598–1605, 1994.
- [37] N. E. Murray and L. S. Ukeiley. An application of gappy pod: For subsonic cavity flow piv data. *Experiments in Fluids*, 42:79–91, 2007.
- [38] A. Nekkanti and O. T. Schmidt. Gappy spectral proper orthogonal decomposition. *Journal of Computational Physics*, 478:111950, 2023.
- [39] M. A Oliver and R. Webster. Kriging: a method of interpolation for geographical information systems. *International Journal of Geographical Information System*, 4(3):313–332, 1990.
- [40] S. V. Patankar and D. B. Spalding. A calculation procedure for heat, mass and momentum transfer in three-dimensional parabolic flows. In *Numerical prediction of flow, heat transfer, turbulence and combustion*, pages 54–73. Elsevier, 1983.
- [41] W. Peng, G. Li, J. Geng, and W. Yan. A strategy for the partition of mrf zones in axial fan simulation. *International Journal of Ventilation*, 18(1):64–78, 2019.
- [42] R. W. Reynolds and T. M. Smith. Improved global sea surface temperature analyses using optimum interpolation. *Journal of climate*, 7(6):929–948, 1994.
- [43] Matteo Ripepi, Mark Johannes Verveld, NW Karcher, Thomas Franz, Mohammad Abu-Zurayk, Stefan Götz, and Thiemo M Kier. Reduced-order models for aerodynamic applications, loads and mdo. *CEAS Aeronautical Journal*, 9(1):171–193, 2018.
- [44] R. Rojas and R. Rojas. The backpropagation algorithm. *Neural networks: a systematic introduction*, pages 149–182, 1996.
- [45] D. E. Rumelhart, G. E. Hinton, and R. J. Williams. Learning representations by back-propagating errors. *nature*, 323(6088):533–536, 1986.
- [46] C. L. Rumsey. Compressibility considerations for kw turbulence models in hypersonic boundary-layer applications. *Journal of Spacecraft and Rockets*, 47(1):11–20, 2010.
- [47] Sajad Salavatidezfouli, Armin Sheidani, Kabir Bakhshaei, Ali Safari, Arash Hajisharifi, Giovanni Stabile, and Gianluigi Rozza. Modal analysis of the wake shed behind a horizontal axis wind turbine with flexible blades. *Journal of Applied and Computational Mechanics*, 11(3):826–843, 2025.
- [48] V. Sekar, Q. Jiang, C. Shu, and Boo C. Khoo. Fast flow field prediction over airfoils using deep learning approach. *Physics of Fluids*, 31(5), 2019.
- [49] S. Sharma, Simone S., and A. Athaiya. Activation functions in neural networks. *Towards Data Sci*, 6(12):310–316, 2017.
- [50] T. M. Smith, R. W. Reynolds, R. E. Livezey, and D. C. Stokes. Reconstruction of historical sea surface temperatures using empirical orthogonal functions. *Journal of Climate*, 9(6):1403–1420, 1996.
- [51] E. Söylemez, E. Alpman, A. Onat, and S. Hartomacıoğlu. Cfd analysis for predicting cooling time of a domestic refrigerator with thermoelectric cooling system. *International Journal of Refrigeration*, 123:138–149, 2021.
- [52] H. G. Weller, G. Tabor, H. Jasak, and C. Fureby. A tensorial approach to computational continuum mechanics using object-oriented techniques. *Computers in physics*, 12(6):620–631, 1998.
- [53] D. C. Wilcox. Formulation of the kw turbulence model revisited. *AIAA journal*, 46(11):2823–2838, 2008.
- [54] K. Willcox. Unsteady flow sensing and estimation via the gappy proper orthogonal decomposition. *Computers & fluids*, 35(2):208–226, 2006.

- [55] Shijie Xu, Min Wang, Lili Han, Shoujie Zhang, Jianlin Yu, and Suxin Qian. A co-simulation method of refrigerator system and temperature field. *Applied Thermal Engineering*, 235:121412, 2023.
- [56] A. Yakhot, T. Anor, and G. E.m. Karniadakis. A reconstruction method for gappy and noisy arterial flow data. *IEEE transactions on medical imaging*, 26(12):1681–1697, 2007.
- [57] M. Z Yousif, L. Yu, S. Hoyas, R. Vinuesa, and H. Lim. A deep-learning approach for reconstructing 3d turbulent flows from 2d observation data. *Scientific Reports*, 13(1):2529, 2023.
- [58] C. Zhang and Y. Lian. Conjugate heat transfer analysis using a simplified household refrigerator model. *International journal of refrigeration*, 45:210–222, 2014.